Chapter 10

Plasma Generation and Application in a Laser Ablation Pulsed Plasma Thruster

Jianjun Wu, Yu Zhang, Yuqiang Cheng, Qiang Huang, Jian Li and Xiaobin Zhu

Additional information is available at the end of the chapter

http://dx.doi.org/10.5772/intechopen.77511

Abstract

The laser ablation plasma thruster is a novel electric propulsion thruster, which combined the laser ablation and electromagnetic acceleration. In order to investigate the plasma expansion and ionization in the laser ablation plasma thruster, which was difficult to obtain from experiments, the heat conduction model and fluid dynamics model were established. The heat conduction model was established to calculate the target ablation, taking into account temperature-dependent material properties, phase transition, dielectric transition and phase explosion. The fluid dynamics model was used to calculate the plasma properties, taking into account ionization, plasma absorption and shielding. The ablation plasma velocity, temperature and electron number density were predicted by using the numerical method. The calculated results showed that the peak values of ablation plasma velocity, temperature and electron number density fraction were distributed at the front of the plasma plume. Moreover, the discharge characteristics and thrust performance were tested with different charged energy, structural parameters and propellants. The thrust performance was proven to be improved by electromagnetic acceleration.

Keywords: laser ablation plasma thruster, heat conduction, plasma expansion, ionization, discharge, thrust performance

1. Introduction

Because of the advantages of low-cost, low-mass, and high specific impulse, electric propulsion thrusters (EPTs) for spacecraft orbit correction and interplanetary spacecraft acceleration have recently become the front subject and focal point in space propulsion fields [1, 2]. As a

member of EPTs, pulsed plasma thruster (PPT) has a broad prospect on small satellites for its small, compact, and low mass [3–5]. PPT has been studied decades on its performance and lifetime, and has been successfully applied to a number of satellites [6–8]. However, the problem of low efficiency and ignition failure still restricts the development of PPT.

Early in the year 2000, Horisawa et al. proposed a laser-assisted plasma thruster (LS-PPT), in which a laser-induced plasma was induced through laser beam irradiation onto a solid target and accelerated by electrical means [9–16]. Compared with the conventional PPT, the LS-PPT combines the laser ablation with electromagnetic acceleration means, which can significantly enhance the thrust performance. However, the phenomenon of "late ablation" is still inevitable in the LS-PPT, which significantly reduces the thrust efficiency of the thruster. In order to overcome the shortage of "late ablation," a novel laser ablation plasma thruster (LA-PPT) is proposed [17]. The LA-PPT separates the laser ablation from electromagnetic acceleration through a ceramic tube. As shown in **Figure 1**, the LA-PPT consists of a pair of rectangular electrodes, a ceramic tube and an insulator. The propellant is placed inside the ceramic tube. Because of the unique structure of this thruster, almost all types of solid matter can be applied as the propellant, such as metals, polymers and so on. Because laser-ablation plasma can has a directed initial velocity of tens of kilometers per second, which will be further accelerated by electrical means, a significant specific impulse can be expected [9]. Hence the LA-PPT is a promising candidate for small satellites propulsion, and the physical mechanisms of the thruster should be further investigated. The working process of the LA-PPT can be divided into two stages: laser-induced ablation and plasma-induced discharge. The ablation plasma expansion and ionization in the ceramic tube is the combination of the two stages, and it is crucial to understand the working process of the LA-PPT. However, the ablation plasma expansion and ionization is difficult to be experimentally investigated, especially when it occurs in a ceramic tube. Therefore, we utilize numerical method to investigate the ablation plasma expansion and ionization in the ceramic tube.

By using the numerical method to simulate the ablation plasma expansion and ionization in the ceramic tube, the relevant physics of propellant ablation needs to be implemented. The heating process within a propellant material during the irradiation of the laser pulse can be calculated by taking into account temperature-dependent material properties, melting, phase transition, dielectric transition, phase explosion, and the reflection of the laser beam at the surface of the propellant [18]. In addition, the ablation plasma absorbs part of laser

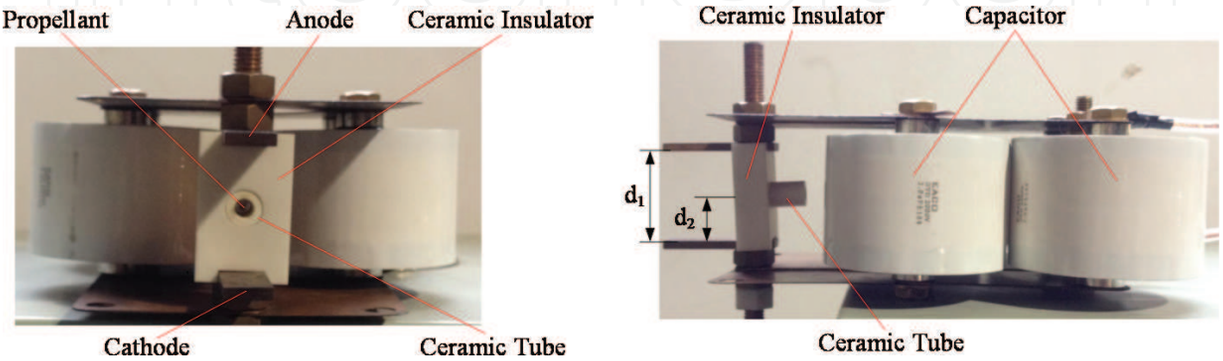

Figure 1. (a) Front and (b) right view of the laser ablation plasma thruster.

http://dx.doi.org/10.5772/intechopen.77511

energy, and causes the density, temperature, pressure and components in the ablation plasma plume dramatically vary, which has an significant effect on the thrust performance. During the years, the expansion dynamics of pulsed laser generated plasma plume has been widely investigated through experimental and numerical methods [19–23]. Especially, several models have been proposed to describe the expansion of ablation plasma and the formation of plasma in the plume [21]. Aden et al. utilized hydrodynamic equations to describe the plasma expansion, which is called hydrodynamic model [24]. Afterwards, the hydrodynamic model had been widely applied to study various laser-solid interactions [25–28]. In order to calculate the laser energy loss caused by plasma absorption and shielding, the formation of plasma in the plume was also considered in several hydrodynamic models [22, 29–32]. Therefore, we establish a hydrodynamic model to investigate the ablation plasma expansion and ionization in the ceramic tube. The numerical model can give insight in the plasma dynamics and plasma behavior of LA-PPT, which is sometimes difficult to obtain from experiments.

In this paper, a novel laser ablation plasma thruster with a ceramic tube is developed and investigated. This thruster is expected to overcome the shortages of conventional laser-electric hybrid acceleration systems in the above paragraph. And the ionization rate, specific impulse and thrust efficiency of the thruster are expected to be increased. Specially, a numerical model for nanosecond laser ablation of aluminum propellant is presented, which contains the target ablation and plasma expansion in the ceramic tube. Heat conduction model is established to calculate the target ablation, taking into account temperature-dependent material properties, phase transition, dielectric transition and phase explosion. Meanwhile, Hydrodynamic model is established to calculate the plasma expansion, taking into account ionization, plasma absorption and shielding. Then both calculations of the target ablation and plasma expansion are coupled in each time step. Afterwards, the plasma properties (such as velocity, temperature and electron number density) in the ceramic tube are numerically investigated utilizing the model. Moreover, the thrust performance of the LA-PPT is also investigated by experimental methods.

2. Physical model

2.1. Heat conduction model

As shown in **Figure 2**, when the laser beam irradiates the target (e.g., aluminum), the temperature in the target rises, and melting occurs when the surface temperature reaches the melting temperature T_m. Then a part of molten materials begins to vaporize when the surface temperature reaches the boiling temperature T_b. With sufficient laser fluence, the target temperature may approach the critical temperature T_c, where dielectric transition occurs, and the dielectric layer is formed near the surface. Furthermore, the ablation plasma expands in the opposite direction of the incident laser beam, and absorbs part of laser energy before the incident laser beam reaches the target surface. The absorption of the laser energy in the plasma accelerates the plasma expansion, at the same time, the shielding of the laser energy by the plasma significantly affect the heat conduction of the target.

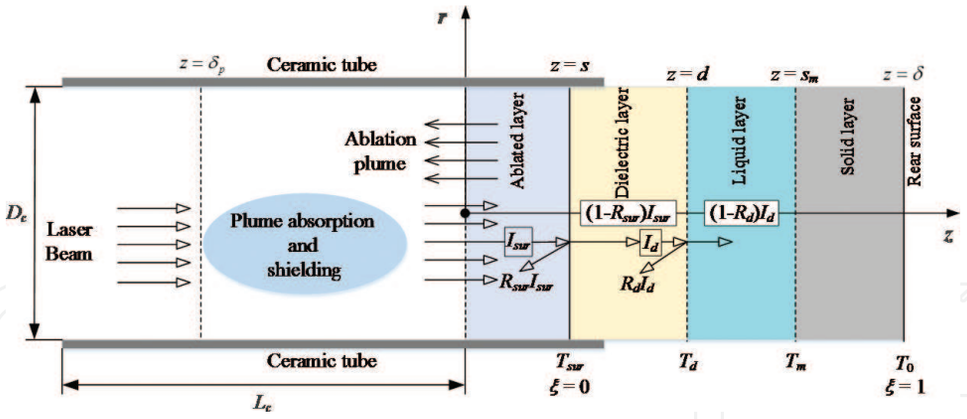

Figure 2. Schematic of the physical model and coordinates.

The initial length of the aluminum target is labeled as δ, as shown in **Figure 2**. The locations of the melting phase interface, the interface between dielectric layer and liquid phase, as well as the exposed ablation surface are labeled as s_m, d, and s, respectively. The length and the inner diameter of the ceramic tube are labeled as L_c and D_c.

The heat conduction equation in terms of the volumetric enthalpy H can be written as:

$$\frac{\partial H}{\partial t}=\frac{\partial}{\partial z}\left(K(T)\frac{\partial T}{\partial z}\right)+v_{sur}(t)\frac{\partial H}{\partial z}+S(t) \tag{1}$$

where $K(T)$ represents the temperature-dependent thermal conductivity. $v_{sur}(t)$ denotes the surface recession velocity, which can be calculated by Hertz-Knudsen [33, 34] and Clausius-Clapeyron equation [35]. The heat source term S is given by:

$$\begin{cases} S(t)=(1-R_{sur})I_{sur}(t)\alpha(t)\exp\left(-\int_{s(t)}^{z}\alpha(t)dz\right), & s(t)\le z\le d(t) \\ S(t)=(1-R_d)I_d(t)\alpha(t)\exp\left(-\int_{d(t)}^{z}\alpha(t)dz\right), & z>d(t) \end{cases} \tag{2}$$

where α is the absorption coefficient of the target, R_{sur} and I_{sur} are the reflectivity and laser intensity on the target surface, respectively. d, R_d and I_d are the location, reflectivity and laser intensity on the interface between dielectric layer and liquid, respectively. Herein, I_{sur} and I_d can be given by:

$$\begin{cases} I_{sur}(t)=I_0(t)\exp\left(-\int_{-\delta_p}^{s(t)}\beta(t)dz\right) \\ I_d(t)=(1-R_{sur})I_{sur}(t)\exp\left(-\int_{s(t)}^{d(t)}\alpha(t)dz\right) \end{cases} \tag{3}$$

where $I_0(t)$ is the initial laser intensity, and β is the absorption coefficient of the plasma.

Considering the regression of the ablation surface, it is more convenient to transform the coordinate (z, t) into the fixed coordinate system (ξ, τ) by the following expressions:

$$\begin{cases} \tau = t \\ \xi = \dfrac{z - s(t)}{\delta - s(t)} \end{cases} \tag{4}$$

As shown in **Figure 2**, $\xi = 0$ (i.e. $z = s(t)$) indicates the ablation surface, and $\xi = 1$ (i.e. $z = \delta$) indicates the rear surface of the target. Moreover, the chain rule can be obtained as follows:

$$\begin{cases} \dfrac{\partial}{\partial z} = \dfrac{1}{\delta - s(t)} \dfrac{\partial}{\partial \xi} \\ \dfrac{\partial}{\partial t} = \dfrac{\partial}{\partial \tau} - \dfrac{\dfrac{\partial s(t)}{\partial t}(1-\xi)}{\delta - s(t)} \dfrac{\partial}{\partial \xi} \end{cases} \tag{5}$$

Combining with Eq. (5), the heat conduction Eq. (1) can be transformed into following form:

$$\frac{\partial H}{\partial \tau} = \frac{1}{(\delta - s)^2} \frac{\partial}{\partial \xi} \left(K \frac{\partial T}{\partial \xi} \right) + \frac{v_{sur}(2-\xi)}{\delta - s} \frac{\partial H}{\partial \xi} + S \tag{6}$$

The initial temperature of the target is considered to be equal to the ambient temperature. The boundary conditions on the rear and side surfaces are considered to be thermal insulation, and the boundary condition on the ablation surface is obtained by energy conservation. Therefore, the initial and boundary conditions are written as:

$$\begin{cases} T(r,z,t)\big|_{t=0} = T_0 \\ \left.\dfrac{\partial T}{\partial z}\right|_{z=\delta} = 0, \; K \left.\dfrac{\partial T}{\partial z}\right|_{z=s(t)} = L_v \rho v_{sur} \end{cases} \tag{7}$$

where T_0 is the initial temperature, L_v is the latent heat of vaporization, and ρ represents the density of the target.

2.2. Plasma expansion and ionization model

The ablation plasma generates with the target ablation, then expands in the opposite direction of the incident laser beam, as shown in **Figure 2**. Part of laser energy deposits in the plasma through inverse bremsstrahlung (IB) absorption, which causes the decrease of the laser intensity reaching on the target surface [31]. In other words, the calculated result of the plasma expansion has an significant effect on the calculation of the target ablation. Moreover, the ionization in the plasma also affects the properties of the plasma. Therefore, the plasma expansion should be calculated in detail, considering the ionization and plasma absorption.

Gas-dynamical equation is used to simulate the plasma expansion, and it can be written as follows:

$$\frac{\partial}{\partial t}\begin{bmatrix}\rho\\ \rho u\\ E\end{bmatrix}+\frac{\partial}{\partial x}\begin{bmatrix}\rho u\\ \rho u^2+p\\ (E+p)u\end{bmatrix}=\begin{bmatrix}0\\ 0\\ S_{plume}\end{bmatrix} \tag{8}$$

where the total energy per unit volume E is the sum of internal energy and kinetic energy.

$$E=\frac{3}{2}\rho\bar{R}T+\sum_{s\neq e}\frac{\rho_s R_s g_1^{(s)}\Theta_{el,1}^{(s)}\exp(-\Theta_{el,1}^{(s)}/T_e)}{\sum_{i=0}^{j^s} g_i^{(s)}\exp(-\Theta_{el,i}^{(s)}/T_e)}+\frac{1}{2}\rho u^2 \tag{9}$$

where ρ denotes density, $\bar{R}=R_0/\bar{M}$, $\bar{M}=\left[\sum(c_s/M_s)\right]^{-1}$, c_s and M_s are the mass fraction and molar mass of species s. $\Theta_{el,i}^{(s)}$ and $g_i^{(s)}$ are the characteristic temperature and degeneracy for species s at electronic energy level i.

The pressure p can be obtained from the state equation:

$$p=\sum_{s=1}^{4}\rho_s R_s T+\rho_e R_e T_e \tag{10}$$

where R_s is molar gas constant of species s, T_e is the temperature of electron.

The initial and boundary conditions of Eq. (7) are determined by the results of target ablation.

The instantaneous laser energy deposition in the plasma S_{plasma} can be calculated as:

$$S_{plasma}(x,t)=I_0(t)\beta(t)\exp\left(-\int_{-\delta_p}^{x}\beta(t)dx\right) \tag{11}$$

where δ_p is the length of the ablation plasma.

In addition, the ionization and IB absorption are considered in the model. In the plasma plume, a local thermodynamic equilibrium stage is assumed. Meanwhile, the plasma plume is considered nonviscous and electrically neutral, containing five species (Al, Al^+, Al^{2+}, Al^{3+}, and e^-). Otherwise, the electron temperature is considered to be equal to the ions and neutrals. Hence, the partition function of species Q^s and Q^e can be expressed as follows:

$$\begin{cases} Q^s=V\left(2\pi m_s k_B T/h^2\right)^{3/2}\sum_{i=0}^{j^s} g_i^{(s)}\exp\left(-\Theta_{el,i}^{(s)}/T\right)\\ Q^e=V\left(2\pi m_e k_B T_e/h^2\right)^{3/2}\end{cases} \tag{12}$$

where m_s denotes the mass of species s, s = Al, Al^+, Al^{2+}, Al^{3+}. V is the plasma plume volume, h is Planck constant.

The species number density n_s can be solved in an equilibrium state [22]:

$$\begin{aligned}
&\frac{n_{\mathrm{Al}^+} n_{\mathrm{e}}}{n_{\mathrm{Al}}} = \frac{Q^{\mathrm{Al}^+} Q^{\mathrm{e}}}{V Q^{\mathrm{Al}}} \exp\left(-\frac{IP_{\mathrm{Al}}}{k_B T}\right) \\
&\frac{n_{\mathrm{Al}^{2+}} n_{\mathrm{e}}}{n_{\mathrm{Al}^+}} = \frac{Q^{\mathrm{Al}^{2+}} Q^{\mathrm{e}}}{V Q^{\mathrm{Al}^+}} \exp\left(-\frac{IP_{\mathrm{Al}^+}}{k_B T}\right) \\
&\frac{n_{\mathrm{Al}^{3+}} n_{\mathrm{e}}}{n_{\mathrm{Al}^{2+}}} = \frac{Q^{\mathrm{Al}^{3+}} Q^{\mathrm{e}}}{V Q^{\mathrm{Al}^{2+}}} \exp\left(-\frac{IP_{\mathrm{Al}^{2+}}}{k_B T}\right) \\
&n_{\mathrm{Al}} + n_{\mathrm{Al}^+} + n_{\mathrm{Al}^{2+}} + n_{\mathrm{Al}^{3+}} + n_{\mathrm{e}} = n_T \\
&n_{\mathrm{Al}^+} + 2n_{\mathrm{Al}^{2+}} + 3n_{\mathrm{Al}^{3+}} = n_{\mathrm{e}}
\end{aligned} \tag{13}$$

Where IP_{Al}, IP_{Al^+} and $IP_{\mathrm{Al}^{2+}}$ are the first, second and third ionization energy of aluminum, respectively.

IB process is considered to be the most important mechanism of the plasma absorption, for nanosecond laser ablation of aluminum [22, 34, 36]. The IB absorption coefficient is given by the sum of the processes between electron and neutral atomic species, and between electron and ions, as follows [22, 37]:

$$\begin{aligned}
&\beta = \beta^{\mathrm{IB}} = \beta^{\mathrm{IB}}_{\mathrm{e\text{-}Al}} + \beta^{\mathrm{IB}}_{\mathrm{e\text{-}i}} \\
&\beta^{\mathrm{IB}}_{\mathrm{e\text{-}Al}} = \left[1 - \exp\left(-\frac{h\nu_l}{k_B T}\right)\right] n_{\mathrm{e}} n_{\mathrm{Al}} Q_{\mathrm{e\text{-}Al}} \\
&\beta^{\mathrm{IB}}_{\mathrm{e\text{-}i}} = \left[1 - \exp\left(-\frac{h\nu_l}{k_B T_{\mathrm{e}}}\right)\right] \frac{4e^6 \lambda_l^3}{3hc^4 m_e} \sqrt{\frac{2\pi}{3m_{\mathrm{e}} k_B T_{\mathrm{e}}}} n_{\mathrm{e}} (n_{\mathrm{Al}^+} + 4n_{\mathrm{Al}^{2+}} + 9n_{\mathrm{Al}^{3+}})
\end{aligned} \tag{14}$$

where υ_l and λ_l are the laser frequency and wave length. Where $Q_{\mathrm{e\text{-}Al}}$ denotes the averaged cross section for a collision between electron and neutral atom (10^{-46} m^5) [22].

Obviously, the absorption coefficient of the plasma β and the length of the plasma plume δ_p are changing, during the laser ablation process. Therefore, it is necessary to calculate the target ablation coupled with the plasma expansion in each time step.

2.3. Numerical method

In the numerical calculation, the length of target and plasma plume are assumed to be 5 and 200 μm. Meanwhile, 400 and 1000 uniform meshes are utilized, respectively, in the target and plasma region. The time-step is taken to be $\Delta t = 10^{-12}$ s, respecting the CFL condition in the entire computational domain.

The heat conduction Eq. (6) is solved employing an explicit finite difference technique. And the gas-dynamical Eq. (8) is diverged utilizing AUSM+-up method [38, 39]. In the numerical calculation, the target ablation and plasma expansion are calculated simultaneously, and coupled in each time step. Since the plasma occurs due to the ablation of target, the ablation surface of target is the inlet of the plasma. Meanwhile, the instantaneous laser intensity reaching on the target surface is decided by plasma absorption.

3. Experimental setup

3.1. Measurement setup for discharge arcs

As shown in **Figure 3**, a ns-pulsed Nd:YAG laser (InnoLas Corp. SpitLight 600, wavelength: 1064 nm, pulse energy: ~600 mJ, pulse width: 7 ns) is used for laser ablation of propellants. The laser pulse is irradiated into a vacuum chamber (vacuum degree: $<5.0 \times 10^{-4}$ Pa) through a quartz window and focused on the propellant with a focusing lens (f = 400 mm). The thruster is ignited and initiated by the ns-pulsed laser. Discharge arcs formed between the electrodes of thruster. The discharge current is monitored with a current monitor (Rogowski Coil, CWT150, sensitivity: 0.2 mV/A, maximum current: 30.0 kA) and a digital oscilloscope (Tektronix DPO 4340). The discharge voltage between the electrodes is measured using a standard high-voltage probe (Tektronix P5100).

3.2. Description of thrust stand

The impulse bits in the six cases of **Table 1** are measured by a calibrated thrust stand. The calibrated thrust-stand utilizing inverted pendulum techniques is developed and applied to estimate μNs-class impulses. Schematic of experimental setup for impulse-bit measurement is given in **Figure 3**. The thruster was settled onto the inverted pendulum. As an ns pulsed Nd:YAG laser beam passes through a quartz glass window and lens, the thruster is initialized, and the plasma is produced. The inverted pendulum swung on a knife-edge immediately. The motion of the pendulum is attenuated by an electromagnetic damper device subsequently. And the pendular angular is measured by an optical non-contacting measurement method. A He-Ne laser beam penetrated through a quartz glass window and irradiated onto a moving mirror settled near the knife-edge. The mirror rotated along with the motion of pendulum. The laser beam eventually irradiates into a position sensitive detector (PSD) after passing through several mirrors as shown in **Figure 3**.

For measuring the impulse bits, the calibration procedures are conducted. Because of the zero drift phenomenon and other influencing factors that gradually change the equilibrium position

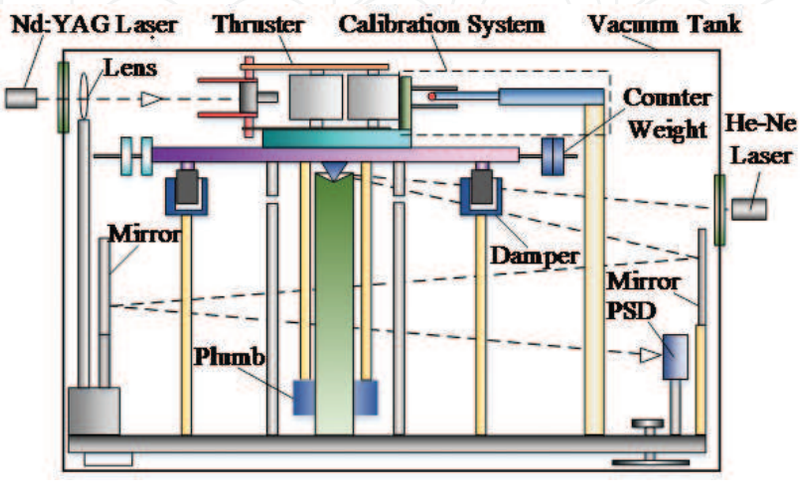

Figure 3. Schematic illustration of the impulse bit measurement system.

http://dx.doi.org/10.5772/intechopen.77511

Case	Propellants	d_1 (mm)	d_2 (mm)	A_0	B_0	A	B
I	Aluminum	20	10	4.8666E−3	5.6211E1	−6.5748E−4	2.2113E−2
II	Aluminum	30	10			−1.2289E−3	2.4758E−2
III	Aluminum	30	15			1.5489E−4	2.5930E−2
IV	Aluminum	30	20			1.0816E−3	2.8182E−2
V	Aluminum	40	20			1.1685E−3	2.8730E−2
VI	PTFE	20	10			3.5247E−3	2.3624E−2

Table 1. Six cases and coefficients obtained in calibration procedures.

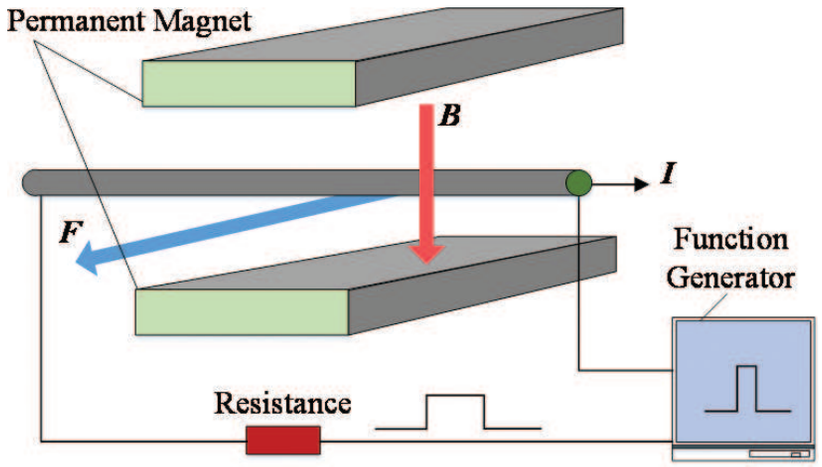

Figure 4. Schematic illustration of the electromagnetic calibration method.

of pendulum in experiments, especially in evacuation and gas charging procedure of the vacuum chamber, the measurement system should be calibrated before or after impulse bit measurements are implemented. The electromagnetic calibration subsystem is proposed as shown in **Figure 4** and described herein. A pulsed Ampere force is generated by a couple of parallel permanent magnet (NdFeB) plates and live wires as shown in **Figure 4**, and utilized to simulate the pulsed thrust of thruster. The pair of permanent magnet plates is settled behind the thruster, and the height of Ampere force action spot is set to be the same with the action spot of pulsed thrust of thruster. The distance between the couple of magnets is set 5 mm, and the crest value and duration of current in the conducting wires are controlled by a function generator as shown in **Figure 4**.

The detailed calibration procedure is described herein.

a. The relationship of Ampere force F and the volts d.c. output X of the function generator is tested by using an electronic balance (Mettler Toledo XS205, minimum mass 10 μg). The relationship can be expressed as:

$$F = A_0 + B_0 X \tag{15}$$

where the coefficients A_0 and B_0 are obtained after the calibration procedure.

b. The calibration devices are settled on the thrust stand with keeping the distance of permanent magnet plates and the relative location between the permanent magnet plates and the conducting wires. And the pendulum is propelled by the Ampere force with duration of t. Therefore, the relationship of PSD signals S and the volts d.c. output X of function generator can be obtained and written as:

$$S = g(X, t) \tag{16}$$

For the sake of simplification and considering that the pendular period of pendulum is generally longer than 5 s in the experiments, the duration of Ampere force t can be set 1 s by the function generator hereafter. Hence, the expression (16) can be expressed as:

$$S = g(X) \tag{17}$$

According to further study, it's indicated that the expression (17) can be simplified as:

$$S = A + BX \tag{18}$$

where, the coefficients A and B in expressions (18) could be obtained in the calibration procedures, as shown in **Table 1**. Besides, according to expression (15), the impulse bit I_b can be expressed as:

$$I_b = Ft = (A_0 + B_0 X)t \tag{19}$$

c. The relationship of impulse bit and PSD signal S can be obtained as:

$$I_b = (S - A)B_0 / B + A_0 \tag{20}$$

The uncertainty analysis is important and conducted herein. There are many sources of error for operating this thrust stand which must be identified, then quantified in order to evaluate the accuracy of the impulse bit measurement. It is shown in the expression (20) that the impulse bit is calculated from the voltage values of PSD signals and the coefficients in calibration procedures, A, A_0, B and B_0. Therefore, the uncertainties in the system data and results can be categorized into two main types. Firstly, the calibration procedures may generate errors for obtaining the coefficients A, A_0, B and B_0. Secondly, the impulse bit measurement is another source of error.

3.3. Measurement for mass shots

The mass shots are measured for the six cases by using an electronic balance (Mettler Toledo XS205, minimum mass 10 μg). It is apparent that the mass shots with different charged energy for a laser pulse energy of 600 mJ are approximately the same for the first five cases in **Table 1**, because of the isolation of laser ablation and discharge processes in the thruster. The typical number of pulse-shots to measure the mass shots is 100 times. The mass consumptions of propellants per shot are tested approximately as 15.7 and 7.8 μg for PTFE and aluminum, respectively. It is remarkable that the ablation of ceramic tube and ceramic insulator is much weak and not considered herein.

A series of experiments are conducted to test the discharge characteristics and the performance parameters, such as impulse bit, and specific impulse. The experiments are conducted in six cases, as shown in **Table 1**.

4. Results and discussion

4.1. Plasma expansion and ionization

In order to describe the whole process of ablation plasma expansion and ionization, the properties of the plasma at several specific times should be investigated in detail, such as 3.5 ns (the ablation plasma produced), 10.5 ns (the phase explosion finished), 20 ns (the target ablation finished), 60.5 ns (the ablation plasma reaches the wall of the ceramic tube), 100 ns and 200 ns. By solving the gas-dynamical Eq. (8), the plasma velocity, temperature and electron number density fraction can be numerically calculated.

The spatial distribution of plasma velocity along the centerline of the ceramic tube for different times are presented in **Figure 5(a)**, and the variety of the peak plasma velocity with time is presented in the **Figure 5(b)**. It can be seen from **Figure 5(a)**, the peak plasma velocity appears at the front of the plasma. At 3.5 ns, the plasma has ejected from the target, and the peak velocity is about 2400 m/s. Afterwards, the phase explosion occurs at the target surface, and the ablation products carry out lots of heat from the target to the plasma. Hence the plasma velocity quickly increases, due to the phase explosion and the absorption of the laser energy. Thus at 10.5 ns, the peak plasma velocity increases to 4000 m/s. When the target ablation is finished (at 20 ns), the peak plasma velocity is around 4600 m/s. After finishing the target ablation, the plasma velocity still increases. But the increasing rate of the plasma velocity gradually decrease as shown in **Figure 5(b)**, due to the absence of the absorption of the laser energy and the injection of the ablation products.

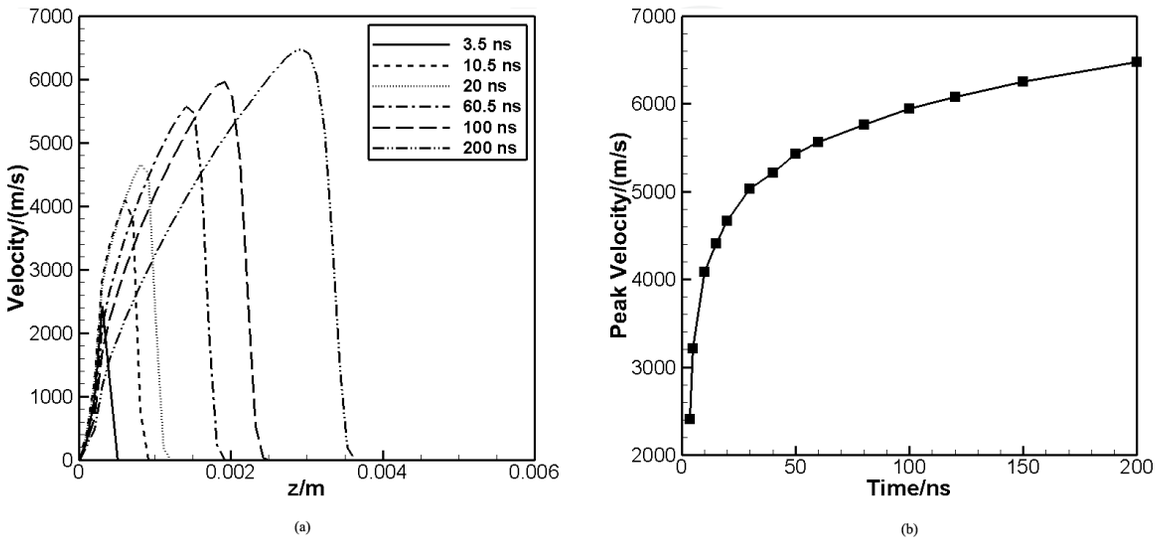

Figure 5. (a) Distribution of plasma velocity for different times. (b) Variety of the peak velocity with time.

The spatial distribution of plasma temperature along the centerline of the ceramic tube for different times are presented in **Figure 6(a)**. The variety of peak plasma temperature with time is presented in **Figure 6(b)**. As can be seen in **Figure 6(a)**, there are two peaks of the plasma temperature appears nearby the target surface (T_1) and at the front of the plasma (T_2). T_1 is due to the high-temperature ablation products ejection from the target to the plasma. T_2 is because of the plasma absorption of laser energy through IB absorption, which causes the plasma temperature to increase. At 3.5 ns, only T_1 exists and equals to 4500 K, due to the injection of high-temperature ablation products. However, afterwards, both T_1 and T_2 appear in the figure. The T_1 gradually increases to about 5700 K at 10.5 ns, and then decreases to below 2000 K at 200 ns. We can also conclude from **Figure 6(b)**, the variation tendency of T_1 is consistent with the target temperature. The T_1 decreases after 10.5 ns. However, the T_2 sharply increases during the laser pulse (from 3.5 to 20 ns), and then nearly keep constant after finishing the laser pulse (20 ns). Thus at 200 ns, only T_2 exists in the figure. What is coincident, the T_1 equals to T_2 at 15 ns, therefore the T_1 is bigger than T_2 before 15 ns and smaller than T_2 after 15 ns.

The spatial distribution of plasma electron number density fraction (η) along the centerline of the ceramic tube for different times are presented in **Figure 7(a)**. The variety of the fraction (ψ) of ionization area to the whole ceramic tube area with time is presented in **Figure 7(b)**. As it can be seen in **Figure 7(a)**, the ionization region mainly distributes at the front of the plasma, which is similar to the plasma velocity and temperature. The η increases during the laser pulse, and at 20 ns, the peak η approaches 0.5, which means the plasma is fully ionized at this region. Afterwards, the η keep constant at 0.5, but the area of the fully ionized region continuously increases. However, only primary ionization occurs in the plasma, due to the equilibrium relations of $\eta_{Al} + \eta_{Al^+} + \eta_{Al^{2+}} + \eta_{Al^{3+}} + \eta_e = 1$ and $\eta_{Al^+} + 2\eta_{Al^{2+}} + 3\eta_{Al^{3+}} = \eta_e$. We can also conclude from the **Figure 7(b)**, the ψ increases faster during the laser pulse, from 1% at 3.5 ns to 3% at 20 ns. Afterwards, the increasing rate of the ψ gradually decreases, at 200 ns, the ψ approaches 6%.

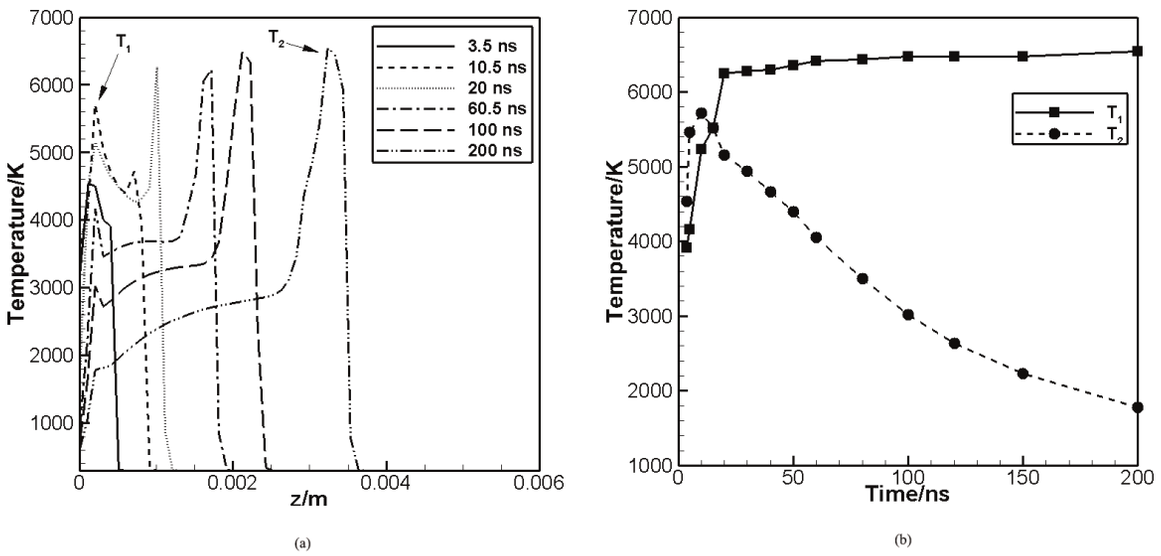

Figure 6. (a) Distribution of plasma temperature for different times. (b) Variety of peak temperature with time.

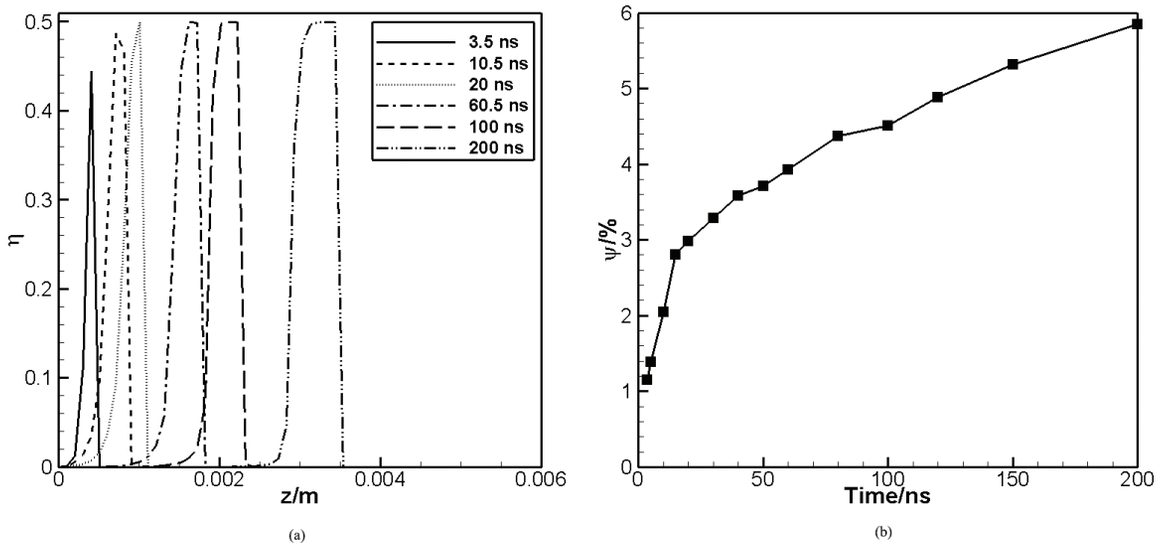

Figure 7. (a) Distribution of plasma electron number density fraction (η) for different times. (b) Variation of the fraction (ψ) of ionization area to the whole ceramic tube area with time.

4.2. Thrust performances

The impulse bits and discharge currents were measured with different parameters d_1 and d_2. Temporal variations of discharge current between the electrodes for charged voltage conditions from about 300 to 2000 V and a laser pulse energy of 600 mJ are shown in **Figure 8** respectively. The impulse bits in different cases are shown in **Figure 9**.

It is shown in **Figure 8** that the higher the charged energy, the higher the discharge current being achieved. In the case I, a maximal charged energy is 25.2 J, d_1 = 20 mm, d_2 = 10 mm and the propellant is aluminum. It is shown that the peak value of discharge current under the charged voltage of 2050 V is more than 20 kA. And it is proven that discharge current can be observed under very low charged voltage conditions (~316 V), in which case a discharge current raises up to 2.7 kA at 1.1 μs. Compared between **Figure 8(a)** and **(b)**, it can be concluded that the peak value of discharge current decrease as d_1 increasing for the situation of same charged voltage. Compared between **Figure 8(b)–(d)**, it can be concluded that the peak value of discharge current reaches maximum for the situation of $d_1 = 2d_2$, which means the propellant is placed in the middle of the electrodes.

The specific impulse and thrust efficiency could be calculated from the impulse bits and mass shots tested for the six cases. The curves of specific impulse for each working condition are illustrated as shown in **Figure 9**. In addition, the thrust efficiency of the thruster is defined as:

$$\eta = E_{kinetic} / E_{total} = 10^3 I_b^2 / (2mE_{total}) \tag{21}$$

where E_{total} is the total energy imported by the thruster, consisting of the single laser energy and the charged energy of capacitors, i.e., $E_{total} = E_{laser} + E_{charge}$. I_b represents the impulse bit, m is the mass ablated per shot and v is the mean velocity of plasma. And the factor 10^3 is required in the conversion of units. The thrust efficiency η was calculated and listed in **Figure 10**.

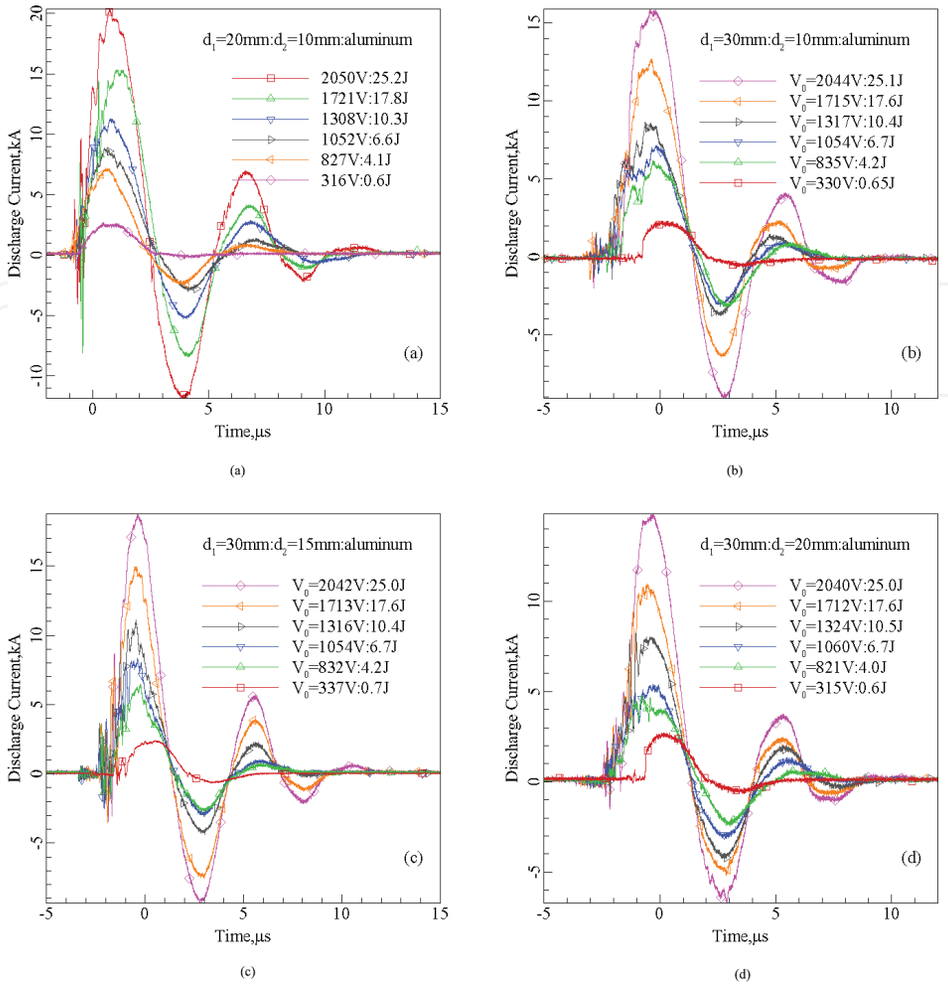

Figure 8. Discharge current between electrodes with different structural parameters: (a) case I, (b) case II, (c) case III and (d) case IV.

The impulse bits and specific impulses of thruster increase with the charged energy of capacitors, as shown in **Figures 9** and **10**. However, the thrust efficiency in case V decreases with the increment of charged energy in the range of 6–10 J, as shown in **Figure 11**. The rate of change of specific impulse or the thrust efficiency to charged energy is much smaller than at the higher energy levels.

Maximal specific impulse, impulse bit and thrust efficiency are achieved with a charged energy of above 25 J for all cases, as shown in **Figures 9–11**. For the case III, with a charged energy 25 J and the use of metal aluminum, a maximal impulse bit of 600 μNs, a specific impulse of approximate 8000 s and thrust efficiency of about 90% are obtained.

In addition, when the charged voltage is decreased to 0 V, the status can be called as the pure laser propulsion mode. And status with a charged voltage above zero is called as electromagnetic acceleration mode. The left ends of curves in **Figure 6** represent the impulse bit with low charged energy levels and that the discharge processes are weak, and the impulse bits equal approximately with the impulse bits in pure laser propulsion modes.

http://dx.doi.org/10.5772/intechopen.77511

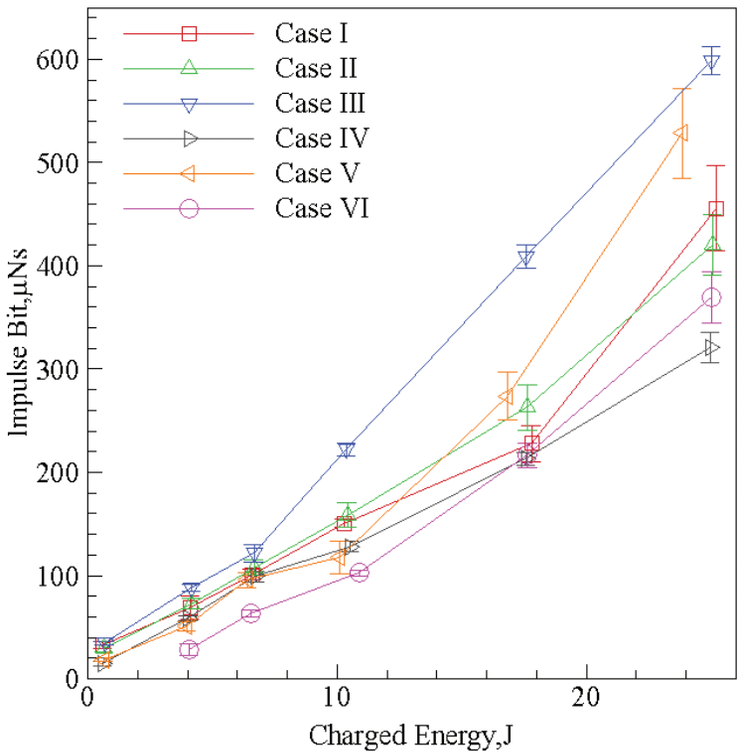

Figure 9. Variations of impulse bit with charged energy.

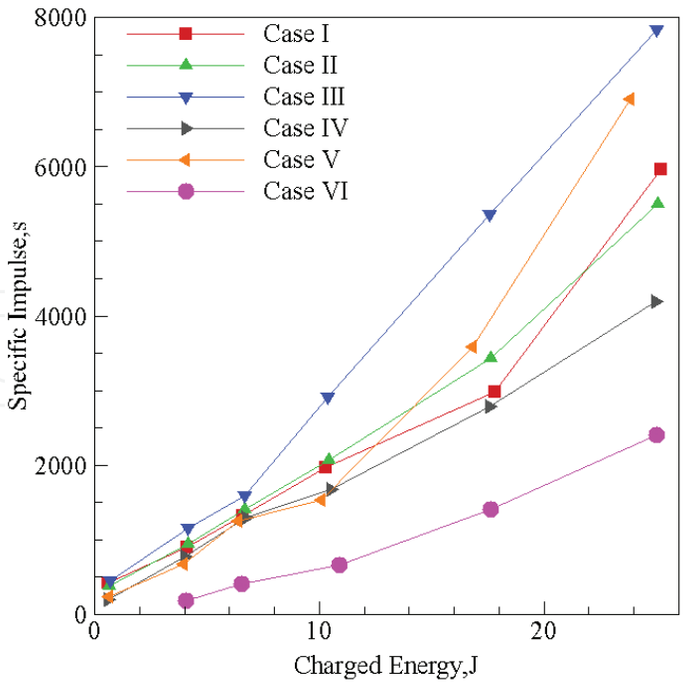

Figure 10. Variations of specific impulse with charged energy.

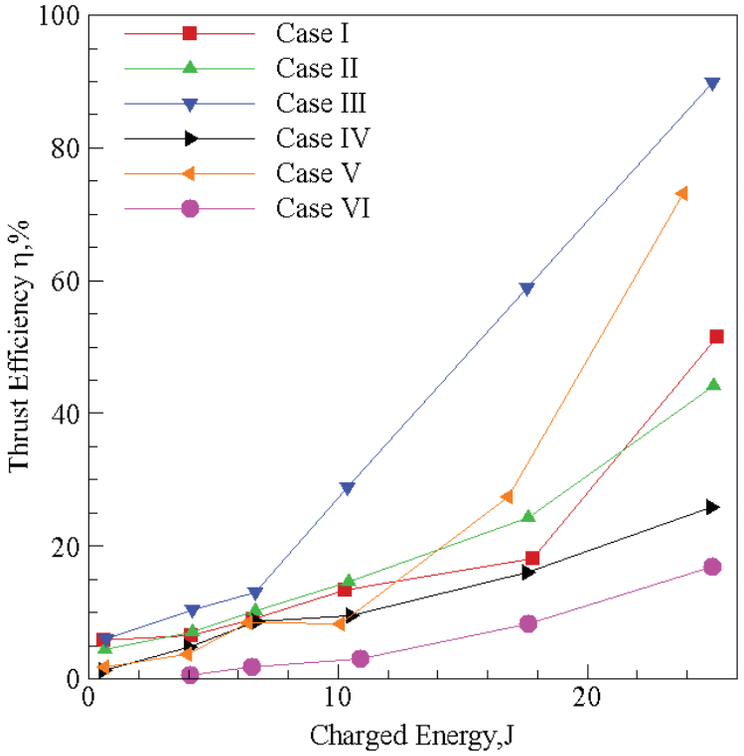

Figure 11. Variations of thrust efficiency with charged energy.

As shown in **Figure 9**, the impulse bit in pure laser propulsion mode can be estimated as 10–30 μNs with an approximate specific impulse of 100–300 s and thrust efficiency of 1–4%. In contrast with the pure laser propulsion mode, the thrust performance in electromagnetic acceleration mode is much better. It is apparent that the discharge processes do enhance and accelerate the laser plasma. And the thrust performance is proven to be improved by the electromagnetic acceleration.

5. Discussion

In this paper, a novel laser ablation plasma thruster with electromagnetic acceleration is presented. The plasma expansion and ionization induced by nanosecond pulsed laser in a ceramic tube are investigated by using the numerical method. The heat conduction model and fluid dynamics model are established to calculate the target ablation and plasma properties. Moreover, a rectangular electrode configuration with several capacitors and a ceramic tube is used, which allows the metals to be used as propellants. Preliminary experiments on the discharge characteristics and thrust performance are conducted and analyzed. Following conclusions are achieved and summarized.

1. Along the centerline of the ceramic tube, the peak values of plasma velocity, temperature and electron number density fraction distribute at the front of the plasma. The plasma velocity increases with time, but the increasing rate gradually decreases.

2. There are two peaks of the plasma temperature appear in the plasma along the centerline of the ceramic tube. The peak temperature nearby the target is due to the injection of the high-temperature ablation products. Hence its variation tendency is consistent with the target temperature. The peak temperature exist at front of the plasma is because of the IB absorption of the laser energy. Hence it increases during the laser pulse, and keep constant after finishing the laser pulse.
3. The plasma electron number density fraction increases during the laser pulse, and approaches 0.5 when the laser pulse finished, which means fully ionized in this region. After finishing the laser pulse, the plasma electron number density fraction keep constant, but the area of the fully ionized region continuously increases.
4. The thrust performance is proven to be improved by the electromagnetic acceleration. In contrast with the pure laser propulsion mode, the thrust performance of electromagnetic acceleration modes is much better.
5. The impulse bit and specific impulse increased with the charged energy. The optimal thrust performance of the thruster in experiments exists in large charged energy modes. With the charged energy 25 J and the use of metal aluminum, a maximal impulse bit of 600 μNs, a specific impulse of approximate 8000 s and thrust efficiency of about 90% are obtained. For the PTFE propellant, a maximal impulse bit of about 350 μNs, a specific impulse of about 2400 s, and thrust efficiency of about 16% are obtained.

Acknowledgements

The authors would like to thank National Natural Science Foundation of China for the financial assistance provided under the grant numbers 11772354 for this work.

Author details

Jianjun Wu*, Yu Zhang, Yuqiang Cheng, Qiang Huang, Jian Li and Xiaobin Zhu

*Address all correspondence to: jjwu@nudt.edu.cn

College of Aerospace Science and Engineering, National University of Defense Technology, Changsha, Hunan, China

References

[1] Pozwolski A. Electromagnetic propulsion of satellites. Acta Astronautica. 2008;**63**:575-577. DOI: 10.1016/j.actaastro.2008.03.018

[2] Silnikov MV, Kulakov KS, Kulakov SL, et al. Correction thruster development based on high-current surface discharge in vacuum. Acta Astronautica. 2015;**109**:177-181. DOI: 10.1016/j.actaastro.2014.10.021

[3] Zhang R, Zhang DX, Zhang F, et al. Deposition of fluorocarbon films by pulsed plasma thruster on the anode side. Applied Surface Science. 2013;**270**:352-358. DOI: 10.1016/j.apsusc.2013.01.029

[4] Hou DL, Zhao WS, Kang X. Operation analysis of pulsed plasma thruster. Acta Astronautica. 2008;**62**:404-409. DOI: 10.1016/j.actaastro.2008.01.004

[5] Burton RL, Turchi PJ. Pulsed plasma thruster. Journal of Propulsion and Power. 1998; **14**(5):716-735. DOI: 10.2514/2.5334

[6] Schonherr T, Nees F, Arakawa Y, et al. Characteristics of plasma properties in an ablative pulsed plasma thruster. Physics of Plasmas. 2013;**20**(033503):1-8. DOI: 10.1063/1.4794198

[7] Krejci D, Seifert B, Scharlemann C. Endurance testing of a pulsed plasma thruster for nanosatellites. Acta Astronautica. 2013;**91**:187-193. DOI: 10.1016/j.actaastro.2013.06.012

[8] Pottinger SJ, Krejci D, Scharlemann CA. Pulsed plasma thruster performance for miniaturised electrode configurations and low energy operation. Acta Astronautica. 2011;**68**: 1996-2004. DOI: 10.1016/j.actaastro.2010.11.011

[9] Horisawa H, Kimura I. Characterization of novel laser particle accelerators for space propulsion. In: 36th AIAA/ASME/SAE/ASEE Joint Propulsion Conference and Exhibit. Huntsville, Alabama; 16–19 July 2000. p. 36687

[10] Matsubara K, Hosokawa H, Akashi N, et al. A short-pulse laser-assisted pulsed plasma thruster. In: 51st AIAA/SAE/ASEE Joint Propulsion Conference; Orlando, FL; 27–29 July 2015; p. 4183

[11] Akashi N, Oigawa Y, Hosokawa H, et al. Plasma acceleration characteristic of a rectangular laser-electromagnetic hybrid thruster. In: 50th AIAA/ASME/SAE/ASEE Joint Propulsion Conference; Cleveland, OH; 28–30 July 2014; p. 3538

[12] Ono T, Uchida Y, Horisawa H, et al. Measurement of ion acceleration characteristics of a laser-electrostatic hybrid microthruster for space propulsion applications. Vacuum. 2009; **83**:213-216. DOI: 10.1016/j.vacuum.2008.03.098

[13] Ono T, Uchida Y, Horisawa H. Laser-electrostatic acceleration characteristics of a laser-electric hybrid thruster. In: 44st AIAA/ASME/SAE/ASEE Joint Propulsion Conference; Hartford, CT; 21–23 July 2008; p. 5008

[14] Horisawa H, Kawakami M, Kimura I. Laser-assisted pulsed plasma thruster for space propulsion applications. Applied Physics A. 2005;**81**:303-310. DOI: 10.1007/s00339-005-3210-8

[15] Horisawa H, Igari A, Uchida Y, et al. Electrostatic acceleration mode of laser-electric hybrid thrusters. In: 41st AIAA/ASME/SAE/ASEE Joint Propulsion Conference; Tucson, Arizona; 10–13 July 2005; p. 3697

[16] Horisawa H, Kimura I. Fundamental study on laser plasma accelerator for propulsion applications. Vacuum. 2002;**65**(3–4):389-396. DOI: 10.1016/S0042-207X(01)00447-X

[17] Zhang Y, Zhang D, Wu J, et al. A novel laser ablation plasma thruster with electromagnetic acceleration. Acta Astronautica. 2016;**127**:438-447. DOI: 10.1016/j.actaastro.2016.05.039

[18] Zhang Y, Zhang D, Wu J, et al. A thermal model for nanosecond pulsed laser ablation of aluminum. AIP Advances. 2017;**7**(075010):1-15. DOI: 10.1063/1.4995972

[19] Zhao XT, Tang F, Han B, et al. The influence of laser ablation plume at different laser incidence angle on the impulse coupling coefficient with metal target. Journal of Applied Physics. 2016;**120**(213103):1-8. DOI: 10.1063/1.4971247

[20] Liu T, Gao X, Hao Z, et al. Characteristics of plasma plume expansion from Al target induced by oblique incidence of 1064 and 355 nm nanosecond Nd:YAG laser. Journal of Physics D: Applied Physics. 2013;**46**(485207):1-6. DOI: 10.1088/0022-3727/46/48/485207

[21] Annemie B, Maryam A, David A, et al. Computer simulations of laser ablation, plume expansion and plasma formation. Advanced Materials Research. 2011;**227**:1-10. DOI: 10.4028/www.scientific.net/AMR.227.1

[22] Sakai T. Impulse generation on aluminum target irradiated with Nd:YAG laser pulse in ambient gas. Journal of Propulsion and Power. 2009;**25**(2):406-414. DOI: 10.2514/1.37767

[23] Cowpe JS, Pilkington RD, Astin JS, et al. The effect of ambient pressure on laser-induced silicon plasma temperature, density and morphology. Journal of Physics D: Applied Physics. 2009;**42**(165202):1-8. DOI: 10.1088/0022-3727/42/16/165202

[24] Adent M, Beyer E, Herziger G, et al. Laser-induced vaporization of a metal surface. Journal of Physics D: Applied Physics. 1992;**25**:57-65. DOI: 10.1088/0022-3727/25/1/008

[25] Gnedovets AG, Gusarov AV, Smurov I. A model for nanoparticles synthesis by pulsed laser evaporation. Journal of Physics D: Applied Physics. 1999;**32**:2162-2168. DOI: 10.1088/0022-3727/32/17/305

[26] Gusarov AV, Gnedovets AG, Smurov I. Two-dimensional gas-dynamic model of laser ablatin in an ambient gas. Applied Surface Science. 2000;**154-155**:66-72. DOI: 10.1016/S0169-4332(99)00389-X

[27] Gusarov AV, Gnedovets AG, Smurov I, et al. Simulation of nanoscale particles elaboration in laser-produced erosive flow. Applied Surface Science. 2000;**154-155**:331-336. DOI: 10.1016/S0169-4332(99)00451-1

[28] Colonna G, Casavola A, Giacomo A D, et al. Ablation of titanium metallic targets: A comparison between theoretical and experimental results. In: 33rd AIAA Plasmadynamics and Lasers Conference; Maui, Hawaii; 20–23 May 2002 p. 2159

[29] Tillack M, Blair D, Harilal SS. The effect of ionization on cluster formation in laser ablation plumes. Nanotechnology. 2004;**15**:390-403. DOI: 10.1088/0957-4484/15/3/028

[30] Bogaerts A, Chen Z. Effect of laser parameters on laser ablation and laser-induced plasma formation: A numerical modeling investigation. Spectrochimica Acta Part B. 2005;**60**:1280-1307. DOI: 10.1016/j.sab.2005.06.009

[31] Chen Z, Bleiner D, Bogaerts A. Effect of ambient pressure on laser ablation and plume expansion dynamics: A numerical simulation. Journal of Applied Physics. 2006;**99**(063304): 1-9. DOI: 10.1063/1.2182078

[32] Tan X, Zhang D, Li XA, et al. A new model for studying the plasma plume expansion property during nanosecond pulsed laser deposition. Journal of Physics D: Applied Physics. 2008;**41**(035210):1-8. DOI: 10.1088/0022-3727/41/3/035210

[33] Lu Q, Mao SS, Mao X, et al. Theory analysis of wavelength dependence of laser-induced phase explosion of silicon. Journal of Applied Physics. 2008;**104**(083301):1-7. DOI: 10.1063/1.2978369

[34] Bulgakova NM, Bulgakov AV. Pulsed laser ablation of solids: Transition from normal vaporizaiton to phase explosion. Applied Physics A. 2001;**73**:199-208. DOI: 10.1007/s003390000686

[35] Lide DR. CRC Handbook of Chemistry and Physics. 84th ed. CRC press; 2004

[36] Ghalamdaran S, Parvin P, Torkamany MJ, et al. Two-dimensional simulation of laser ablation with 235 nanosecond pulses. Journal of Laser Applications. 2014;**26**(1, 012009):1-8. DOI: 10.2351/1.4847795

[37] Root RG. Modeling of post-breakdown phenomena. In: Rakziemski LJ, Cremers DA, Dekker M, editors. Laser-Induced-Plasmas and Applications. New York; 1989. pp. 69-103

[38] Chang CH, Liou MS. A robust and accurate approach to computing compressible multiphase flow: Stratified flow model and AUSM$^+$-up scheme. Journal of Computational Physics. 2007;**225**:840-873. DOI: 10.1016/j.jcp.2007.01.007

[39] Liou MS. A sequel to AUSM, part II: AUSM$^+$-up for all speeds. Journal of Computational Physics. 2006;**214**:137-170. DOI: 10.1016/j.jcp.2005.09.020